Phase-dependent quantum optical coherence tomography

Mayte Y. Li-Gomez , ^{1,*} Taras Hrushevskyi , ¹ Kayla McArthur , ¹ Pablo Yepiz-Graciano , ² Alfred B. U'Ren , and Shabir Barzanjeh , and Shabir Barzanjeh

¹Institute for Quantum Science and Technology, and Department of Physics and Astronomy, University of Calgary, 2500 University Drive NW, Calgary, Alberta T2N 1N4, Canada

²Instituto de Ciencias Nucleares, Universidad Nacional Autonoma de México, 04510 Ciudad de México, México

(Received 9 March 2025; accepted 19 September 2025; published 10 October 2025)

Two-photon interference is a cornerstone of quantum optics, enabling imaging, sensing, and precision measurements that surpass classical limits. By harnessing the quantum interference of photon pairs, as demonstrated by the Hong-Ou-Mandel effect, this approach offers superior axial resolution and intrinsic dispersion cancellation, along with strong noise suppression arising from the precise temporal correlations between photons. Building on these principles, we present the theoretical framework and experimental realization of phase-dependent quantum optical coherence tomography (QOCT), a technique that employs phase-modulated two-photon interference for noninvasive morphological analysis of multilayered samples. We demonstrate that introducing controlled phase shifts to photon pairs in a Hong-Ou-Mandel interferometer effectively eliminates artifacts caused by reflections at different sample layers, thereby greatly improving the accuracy and reliability of QOCT measurements. This work advances the fundamental understanding and practical deployment of two-photon interference, overcoming a key limitation in applying QOCT to real-world applications such as biomedical imaging and materials characterization.

DOI: 10.1103/nxhw-7nf6

I. INTRODUCTION

Two-photon interference is a fundamental phenomenon in quantum optics, representing one of the manifestations of nonclassical light behavior. When two indistinguishable photons interact at a beam splitter, they exhibit unique interference effects that have no classical analog, enabling transformative applications in quantum information processing [1], quantum sensing [2-6], computing [7,8], and communication [9,10].

Building on this principle, quantum optical coherence tomography (QOCT) [11] extends the capabilities of conventional optical coherence tomography (OCT) by exploiting two-photon interference. OCT is an imaging technique that reconstructs three-dimensional structures by combining lateral beam scanning with low-coherence interferometry, achieving high transverse and axial resolution [12]. In standard OCT, classical light illuminates both arms of a Michelson interferometer, and the image contrast arises from first-order field correlation measurements. In contrast, QOCT replaces classical light with entangled photon pairs generated via spontaneous parametric down-conversion (SPDC) and measures fourth-order field interference, using a Hong-Ou-Mandel

Published by the American Physical Society under the terms of the Creative Commons Attribution 4.0 International license. Further distribution of this work must maintain attribution to the author(s) and the published article's title, journal citation, and DOI.

(HOM) interferometer [13,14]. This quantum enhancement leads to a twofold improvement in axial resolution and cancellation of even-order dispersion [15,16], offering significant advantages for imaging through dispersive media such as biological tissue [17,18].

Despite significant progress and wide-ranging applications, OOCT still faces two main limitations: long acquisition times and the presence of artifacts. These artifacts originate from the quantum properties of the system and are caused by interference between photons reflected from different reflective layers within a sample. In particular, artifacts, along with recently identified echoes [19], appear as peaks or dips in the QOCT signal that do not correspond to actual physical interfaces within the sample. Additionally, for samples with more than two layers, artifacts are generated for every pair of real interfaces, making it increasingly challenging to extract accurate and meaningful information from complex structures. Several approaches have been proposed to mitigate artifacts in QOCT [20-24]; however, all are either very slow or not efficient for practical purposes.

In this work, we introduce phase-dependent QOCT, a technique for artifact-free multilayer sample probing by incorporating phase shifts into correlated photon pairs. This method exploits the phase independence of the HOM effect while leveraging the fact that artifacts originate from cross-interference, which is inherently phase dependent. By modulating the phase of entangled biphotons in tomography, we can effectively control and even eliminate artifacts without affecting the HOM dips corresponding to different layers of the sample. This approach offers several advantages: It requires only minor modifications to conventional two photon-interference-based setups, as it can be implemented

^{*}Contact author: mayte.ligomez@ucalgary.ca

[†]Contact author: shabir.barzanjeh@ucalgary.ca

using standard electro-optic components, and it provides a straightforward yet highly effective solution for artifact management. By overcoming a major limitation of QOCT, this technique improves its suitability for real-world applications, paving the way for implementation and commercialization, and enabling the effective probing of complex multilayered samples such as biological tissues in the eye or skin.

II. EXPERIMENTAL RESULT

Figure 1(a) shows the schematic of the phase-dependent QOCT in which pairs of entangled biphotons, typically generated via the SPDC process, are used as inputs for the HOM interferometer. These photons pass through two phase shifters, each adding a global phase $\phi_i(t) = \beta_i \sin(\Omega_i t + \theta_i)$, with $\beta_i =$ $\frac{V_i}{V_{-i}}\pi$, where V_i is the applied voltage on the electro-optical modulators (EOM) with frequency Ω_i and phase θ_i , with i=1, 2. Here, $V_{\pi,i}$ is the half-wave voltage of the EOM. The idler photon then travels through the reference arm, where a controllable delay τ is introduced, while the signal photon is directed toward the sample arm, where it reflects off various surfaces within the sample. The two photons are then recombined at a beam splitter, where they interfere. The output of their interference $\Gamma(\tau)=1-\frac{G(\tau)}{G_0}$ is recorded as a function of the temporal delay τ between the reference and sample arms (see the Appendix A for the details of the calculations). Here, G_0 represents the self-interference terms that remain independent of τ , while $G(\tau)$ arises from the cross-interference terms and contains HOM dips that encode information about the sample's internal structure, allowing for its morphological properties to be extracted, and it is given by

$$G(\tau) = 2\sum_{mn} \sum_{m'n'} \Lambda_{mn} \Lambda_{m'n'} e^{-\frac{(\Delta_{mn}^+ - \Delta_{m'n'}^+)^2}{2\sigma_d^2}}$$

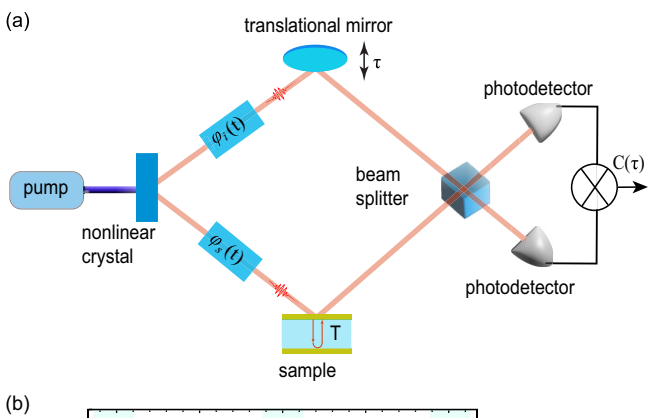
$$\times e^{-\frac{(\Delta_{mn}^- + \Delta_{m'n'}^-)^2}{2\sigma_d^2}} A(T), \tag{1}$$

with

$$A(T) = r_1^2 \kappa(0) + r_2^2 \kappa(T) + r_1 r_2 e^{-\frac{\sigma_d^2}{8} \left(\frac{T}{2}\right)^2} \times \cos\left(\omega_0 T + \frac{(\Delta_{m,n}^+ + \Delta_{m',n'}^+)}{2} \frac{T}{2}\right) \kappa\left(\frac{T}{2}\right), \quad (2)$$

where ω_0 is the pump frequency and σ_a (σ_d) represents the bandwidth along the antidiagonal (diagonal) in the frequency space. In general, σ_a can be experimentally adjusted using a bandpass filter (BPF) applied to the photon pairs, whereas σ_d can be controlled through the pump bandwidth. Additionally, r_1^2 and r_2^2 correspond to the reflectivities of the two layers, and T represents the round-trip time of propagation between them. We also have defined $\Lambda_{mn} \equiv J_m(\beta_1)J_n(\beta_2)$, with $J_m(x)$ being the Bessel functions of the first kind of order m, $\Delta_{m,n}^{\pm} \equiv m\Omega_1 \pm n\Omega_2$, and

$$\kappa(\mathcal{T}) = e^{-\frac{\sigma_a^2}{8}(\mathcal{T} - \tau)^2} \cos\left(\frac{(\Delta_{m,n}^- - \Delta_{m',n'}^-)}{2}(\mathcal{T} - \tau) - \Theta_{m',n'}^{m,n}\right),$$
(3)



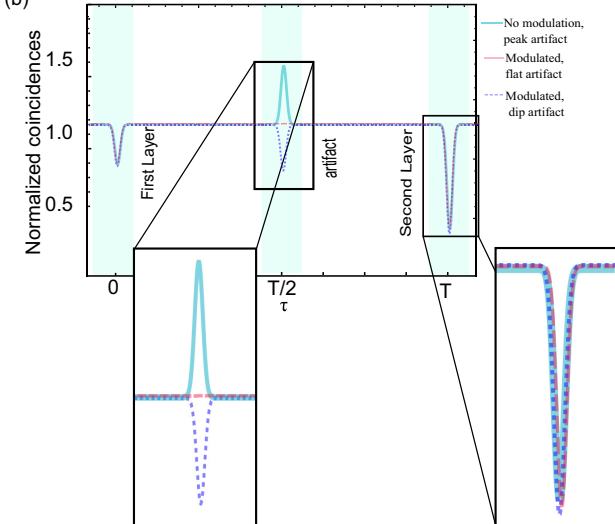


FIG. 1. (a) Schematic of phase-dependent QOCT. Entangled signal-idler photon pairs are generated via the SPDC process when a pump beam interacts with a nonlinear crystal. The generated photon pairs pass through two controllable phase shifters $\phi_i(t)$ before being used to scan a sample. The signal photons then probe different layers of an unknown sample, while the idler photons travel through a reference arm of adjustable length to match the path delay τ with the signal photons. After combining at a beam splitter, the coincidence rate $C(\tau)$ is measured by two photodetectors. (b) Full QOCT coincidence interferogram showing two Hong-Ou-Mandel dips, each corresponding to a reflective layer in a two-layer sample, together with an artifact (center feature). The solid blue-green curve shows the interferogram without phase modulation, where the artifact appears originally as a peak. By varying the phase parameters, the shape and amplitude of the artifact can be modulated, transforming it into a flat (dotted pink) or into a dip (dotted violet) artifact, while the HOM dips remain unaffected. Insets show enlarged views of the stable HOM dips and the artifact.

with $\Theta_{m',n'}^{m,n} \equiv (m-m')\theta_1 + (n-n')\theta_2$. The first two terms in Eq. (2) correspond to the first and second HOM dips, associated with the first layer at $\tau=0$ and the second layer at $\tau=T$, respectively. Meanwhile, the third term represents the artifact that appears at the midpoint of the sample, occurring at $\tau=T/2$. Equation (1) is generally an interesting yet somewhat complex expression. The response of the system has been plotted in Fig. 1(b), which shows the normalized interferogram $\Gamma(\tau)$ for different values of $\beta=\frac{V}{V_{\pi}}\pi$ by changing the applied rf voltages. This figure illustrates that while

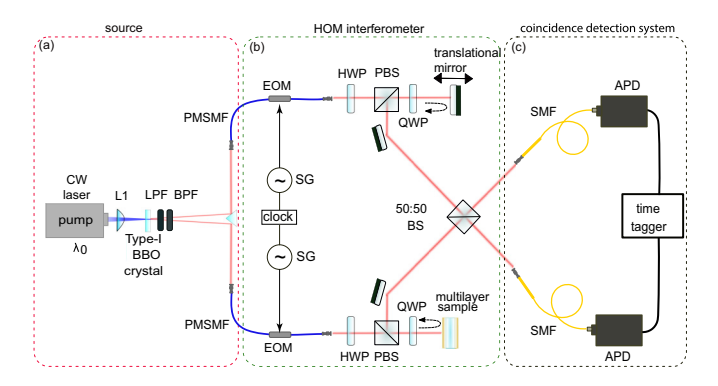


FIG. 2. Phase-dependent QOCT setup: A tunable continuous-wave laser pumps a type-I BBO nonlinear crystal, generating correlated signal-idler photon pairs. The generated pairs pass through two identical EOMs, both driven by locked microwave signal generators (SG). The phase-shifted photon pairs are directed into the HOM interferometer, where they are recombined and subsequently detected using avalanche photodiodes (APDs). Key optical components include PMSMFs, a polarization beam splitter (PBS), a quarter-wave plate (QWP), a beam splitter (BS), long/bandpass filters (L/BPF), a single-mode fiber (SMF), and a half-wave plate (HWP).

the HOM dips remain unchanged, the artifacts can be fully inverted from a peak to a dip or completely suppressed by appropriately tuning the phases. This behavior can be partially understood by focusing only on the diagonal terms in the summation, where n = n' and m = m', leading to

$$G(\tau) = 2\sum_{mn} \Lambda_{mn}^{2} e^{-\frac{2(\Delta_{mn}^{2})^{2}}{\sigma_{d}^{2}}} \left[r_{1}^{2}\kappa(0) + r_{2}^{2}\kappa(T) + r_{1}r_{2}e^{-\frac{(\sigma_{d}^{T})^{2}}{32}} \cos\left(\omega_{0}T + \frac{T\Delta_{m,n}^{+}}{2}\right)\kappa\left(\frac{T}{2}\right) \right].$$
(4)

The above equation explicitly demonstrates that the first and second terms inside the brackets remain unaffected by the phase injected into the photon pairs, whereas the third term depends on $\Delta_{m,n}^+ \equiv m\Omega_1 + n\Omega_2$.

Figure 2 shows the experimental setup for phase-dependent QOCT in which the system is pumped with a tunable continuous-wave (CW) laser, emitting light with a pump wavelength centered at $\lambda_0 = 404.5$ nm. The pump feeds a 2-mm long β -barium borate (BBO) crystal, which generates pairs of photons through type-I SPDC. The phase of each twin photon is independently modulated using EOMs placed at the output of the polarization-maintaining single-mode fibers (PMSMFs). Each modulator is driven by a signal generator SG, which provides a signal with adjustable amplitude, driving rf frequency, and phase difference relative to a common rubidium clock that serves as a reference.

The idler photon is directed to the reference arm, where a temporal delay is introduced and is controlled by adjusting the path-length difference between the idler and signal photons. In the sample arm, the signal photon probes a multilayered sample composed of two reflective interfaces. The sample used in our experiment is 2-mm-thick glass coated at the front and back with a thin gold layer via electron beam deposition. The output beams at the beam splitter's exit ports are coupled into

avalanche photodiode (APDs). The normalized coincidence interferogram $\Gamma(\tau)$, resulting from HOM interference, is measured using a time controller unit with a fixed coincidence window of 2 ns (see the Appendix).

The resulting coincidence interferograms are recorded by independently varying EOM parameters and performing a scan over the temporal delay τ (in ps), corresponding to the optical path length (in μm) traveled by light through the sample. An HOM dip appears in the event that the path-length difference between the reference and sample arms is zero ($\tau=0$), that is, when the signal photon is reflected back from a reflective interface within the sample. While the entire sample length is scannable, our focus is on the region where the artifact appears. Additionally, the front and back surfaces are examined to confirm that the visibility of their respective HOM dips remains unchanged by phase modulation (see the Appendix). This is because the size of the sidebands, determined by the applied frequency and power, is much smaller than the bandwidth of the biphoton state.

Figure 3 illustrates the effect of phase modulation on the artifact for various parameters of both EOMs in the idler (EOM 1) and signal (EOM 2) paths, including the applied voltages (β_i), rf driving frequency Ω_i , and phase difference between the two sources $\Delta\theta=\theta_2-\theta_1$, with i=1,2. Although this experiment uses two EOMs, it should be noted that our protocol does not require both to manipulate the phase. A single EOM can also achieve the desired effect. In each measurement set, we isolate one specific variable and systematically scan its entire range while keeping all other variables constant. The amplitude of the artifact is reported in normalized coincidences $\Gamma(\tau)$.

The voltage scans in Fig. 3(a) are obtained by fixing the driving frequencies at $\Omega_1/2\pi=\Omega_2/2\pi=12.7\,\mathrm{GHz}$ and the phase difference $\Delta\theta=0$. The values of frequency Ω_i and $\Delta\theta$ were specifically selected to achieve the largest change in the amplitude of the artifact and demonstrate the effect of modulation in detail. The polarity of the artifact becomes more negative for higher values of β . Noticeable changes appear at $\beta_1=2.16$ and $\beta_2=1.79$, corresponding to $V_{pp}=2.12\,\mathrm{V}$; the voltage was then gradually increased to the maximum power output of the signal generators at $\beta_1=5.42$ and $\beta_2=4.48$. This led to a full flip on the artifact from peak to dip.

The effect of varying the driving frequencies of both EOMs is shown in Fig. 3(b). The microwave source frequencies for both EOMs are scanned symmetrically, $\Omega_1 = \Omega_2$, over the range of 1–12.7 GHz, while maintaining a fixed phase difference of $\Delta\theta=0$ and applying maximum voltage to each EOM. As seen, the artifact transitions from a peak to a dip and is effectively eliminated at $\Omega_1/2\pi=7$ GHz.

Figure 3(c) illustrates the impact of the phase shift between the EOMs when driven at maximum voltage and a frequency of 12.7 GHz. As with the previous two configurations, the amplitude of the artifact can be controlled, in this case, by adjusting the phase difference $\Delta\theta$. The solid lines in Figs. 3(a)-3(c) show the theoretical fits using Eq. (1).

Finally, the results of the fitting using model based on Eq. (1) for different values of β are shown in Fig. 4. The impact on the visibility of the artifact ($\tau = T/2$) is measured for increasing values of β . The height of the artifact transitions completely from a peak to zero and then to a dip

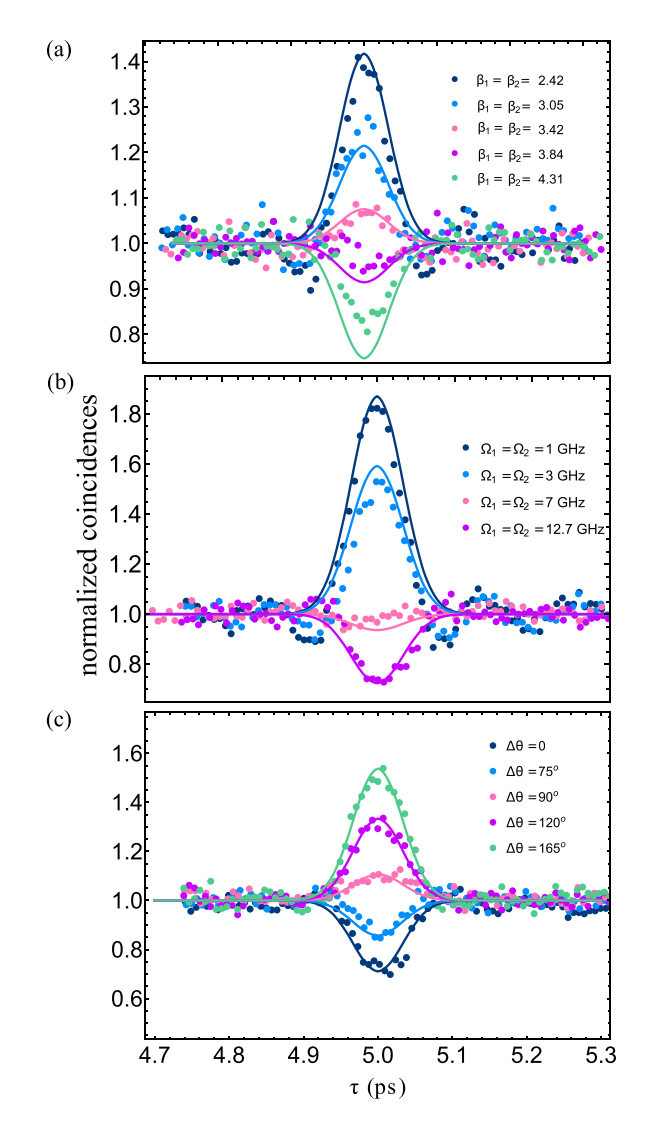


FIG. 3. Effect of modulation parameters on artifact. The height of the artifact, measured in normalized coincidences, varies as a function of (a) the voltage amplitudes β_1 and β_2 , while keeping the driving frequencies fixed at $\Omega_1/2\pi = \Omega_2/2\pi = 12.7$ GHz and the phase difference at $\Delta\theta=0$; (b) the driving frequencies $\Omega_1=\Omega_2$, with a fixed phase difference of $\Delta\theta=0$ and maximum voltage applied to each EOM; and (c) the phase difference between the microwave signals driving the EOMs, when each EOM is driven at maximum voltage at a frequency of 12.7 GHz. Here, the experimental data (dots) have been fitted using our theoretical model (solid line).

by adjusting $\beta = \beta_1 = \beta_2$. In this case, the voltage scans are recorded while keeping the driving frequencies fixed at $\Omega_1/2\pi = \Omega_2/2\pi = 12.7\,\text{GHz}$ and the phase difference $\Delta\theta = 0$. The experimental data (dots) have been fitted using our theoretical model (solid line).

III. SUMMARY

In summary, we have demonstrated that introducing phase shifts to entangled photon pairs enables phase-dependent QOCT, offering a practical and experimentally accessible solution for artifact suppression. Unlike previous approaches

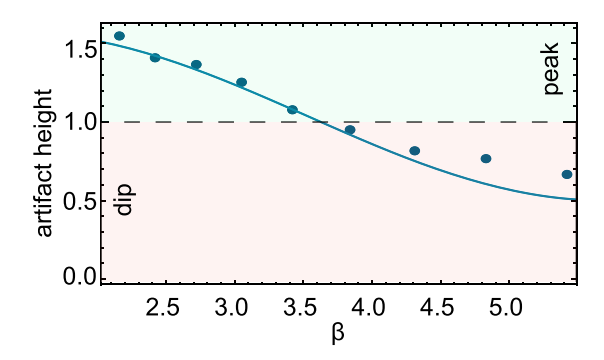


FIG. 4. The artifacts transition from a peak to zero and then to a dip as the modulation depth is adjusted, with $\beta=\beta_1=\beta_2$ for the driving frequencies fixed at $\Omega_1/2\pi=\Omega_2/2\pi=12.7\,\mathrm{GHz}$ and the phase difference at $\Delta\theta=0$. Here, the experimental data (dots) have been fitted using our theoretical model (solid line).

relying on laser frequency tuning, broadband sources, or computationally intensive postprocessing, our method uses externally applied phase modulation to selectively eliminate artifacts without compromising axial resolution. This fundamentally unique mechanism exploits the phase dependence of artifacts versus the phase independence of HOM dips, allowing reliable identification and removal of artifacts for accurate morphological extraction. While effective for simple two-layer samples using a single modulation setting, more complex multilayered samples may require temporal variation of EOM parameters, such as voltage or frequency, to identify artifacts based on their amplitude changes and exclude them during postprocessing. Integration with machine learning or genetic algorithms [19] can further enhance performance by predicting artifact positions and optimizing modulation sequences for efficient suppression across all depths.

While our method addresses a key challenge in OOCT namely, the suppression of artifacts—further improvements are needed to make QOCT viable for real-world applications. Enhancing resolution and acquisition speed remains essential. This can be achieved by tailoring the biphoton spectral distribution, for example, through broader pump bandwidths, thinner nonlinear crystals, or chirped quasiphase matching to optimize frequency correlations. Increasing photon flux using brighter SPDC sources would also accelerate data collection. However, practical deployment still faces challenges, including sensitivity to phase noise in electro-optic modulators and spectral impurities, all of which can degrade artifact suppression and image quality. Although SPDC remains the most widely used source due to its well-characterized entanglement properties and dispersion cancellation, alternative sources, such as four-wave mixing in fibers or engineered quantum dots, could offer greater flexibility, provided that they support suitable spectral correlations.

Beyond QOCT, our results show that phase modulation of entangled photon pairs enables direct control over cross-interference features in quantum measurements, thus introducing a degree of freedom for quantum state manipulation. The artifact amplitude can be leveraged as an indicator of the global phase applied to biphoton states, facilitating potential applications in phase-sensitive quantum metrology, precision probing, and quantum information encoding. This conceptual

insight opens pathways for enhanced quantum sensing protocols and phase-dependent entangled state preparation, topics of strong relevance to the quantum optics community.

ACKNOWLEDGMENTS

We thank Daniel Oblak and Sourabh Kumar, Lindsay LeBlanc, and Erhan Saglamyurek for helping to build the phase modulation part of the experiment. S.B. acknowledges funding by the Natural Sciences and Engineering Research Council of Canada (NSERC) through its Discovery Grant and Quantum Alliance Grant, funding and advisory support provided by Alberta Innovates (AI) through the Accelerating Innovations into CarE (AICE)—Concepts Program, support from Alberta Innovates and NSERC through Advance Grant project, and Alliance Quantum Consortium. This project is funded (in part) by the Government of Canada."

DATA AVAILABILITY

The data supporting this study's findings are available within the article.

APPENDIX A: THEORY OF THE PHASE-DEPENDENT QOCT

We start by introducing the initial quantum state of the entangled photon pairs generated via SPDC:

$$|\psi\rangle = |0\rangle + \eta \iint d\omega_1 d\omega_2 f(\omega_1, \omega_2) |\omega_1\rangle |\omega_2\rangle, \quad (A1)$$

where $f(\omega_1, \omega_2)$ is the joint spectral amplitude (JSA) of the single photons as determined by the phase-matching conditions of the down-conversion process having efficiency η . Note that $S(\omega_1, \omega_2) \equiv |f(\omega_1, \omega_2)|^2$ represents the joint spectral intensity, which describes the probability of detecting a signal photon with frequency ω_1 and an idler photon with frequency ω_2 . This can be approximated as a Gaussian function [19]

$$S(\omega_1, \omega_2) = \frac{4}{\pi \sigma_a \sigma_d} \exp\left[-2\left(\frac{\omega_1 + \omega_2 - 2\omega_0}{\sigma_d}\right)^2\right] \times \exp\left[-2\left(\frac{\omega_1 - \omega_2}{\sigma_a}\right)^2\right], \tag{A2}$$

where ω_0 is the pump frequency and σ_a (σ_d) represents the bandwidth along the antidiagonal (diagonal) in the ω_1, ω_2 frequency space. In general, σ_a can be experimentally adjusted using a BPF applied to the photon pairs, whereas σ_d can be controlled through the pump bandwidth.

We now analyze the effect of applying an external phase to the biphoton state. Assume that an external phase ϕ is applied to each photon in the entangled pair. This is implemented in practice by placing two EOMs along the propagation paths of the biphotons. A sinusoidal electric field drives each EOM with a frequency Ω , where the amplitude of the field proportionally modulates the phase of the transmitted optical field. The additional phase is given by $\phi(t) = \beta \sin(\Omega t + \theta)$, where $\beta = \frac{V}{V_T}\pi$ is the modulation index describing the phase deviation of the modulated signal away from the unmodulated

one, V is the voltage amplitude of the signal, and V_{π} is the half-wave voltage of the EOM. As a result, the output field of the EOM can be expressed as

$$e^{i\phi(t)} = \sum_{m=-\infty}^{\infty} J_m(\beta) e^{im(\Omega t + \theta)},$$
 (A3)

where $J_m(x)$ is the Bessel functions of the first kind of order m. Given that the phases are time dependent, it is practical to analyze the system in the temporal domain, where the JSA of the SPDC photons can be represented as

$$f(\omega_1, \omega_2) = \iint dt_1 dt_2 f(t_1, t_2) e^{-i\omega_1 t_1} e^{-i\omega_2 t_2},$$
 (A4)

where $f(t_1, t_2)$ is the joint temporal amplitude of the biphotons. As a result, the total JSA of the photon pairs after the phase modulation becomes

$$f_{PM}(t_1, t_2) = f(t_1, t_2) \sum_{m = -\infty}^{\infty} J_m(\beta_1) e^{im(\Omega_1 t_1 + \theta_1)}$$

$$\times \sum_{n = -\infty}^{\infty} J_n(\beta_2) e^{in(\Omega_2 t_2 + \theta_2)}.$$
(A5)

In the frequency domain, the phase-shifted JSA can be written as

$$f_{PM}(\omega_1, \omega_2) = \iint dt_1 dt_2 f_{PM}(t_1, t_2) e^{-i\omega_1 t_1} e^{-i\omega_2 t_2}$$

$$= \sum_{m=-\infty}^{\infty} \sum_{n=-\infty}^{\infty} f_{mn}(\omega_1, \omega_2), \tag{A6}$$

where

$$f_{mn}(\omega_1, \omega_2) = f(\omega_1 - m\Omega_1, \omega_2 - n\Omega_2)$$
$$\times J_m(\beta_1)J_n(\beta_2)e^{i(m\theta_1 + n\theta_2)}. \tag{A7}$$

Equation (A6) describes the appearance of multiple sidebands in the spectral space that compose a network of sub-JSAs, f_{mn} , which are separated by integer multiples of the external driving frequency $m\Omega_1$ and $n\Omega_2$.

QOCT takes advantage of HOM interference to reconstruct the internal axial structure of multilayered samples. Pairs of entangled photons, often generated by type-I or type-II SPDC, serve as inputs for the HOM interferomenter. The signal photon is sent to the reference arm with a controllable delay τ , while the idler photon is sent to the sample arm in which light is reflected back from each of the reflective surfaces within the sample. The two photons are then recombined and interfered in a beam splitter. The output of their interference $C(\tau)$ is recorded as a function of the temporal delay between the reference and sample arms. A basic schematic of a QOCT with phase modulation on the entangled pairs is shown in Fig. 1(a). Due to the HOM effect, a dip appears in the interferogram when the optical path lengths of the signal and idler photons are equal. The distance between the HOM dips in the interferogram allows information concerning the sample's internal morphology to be extracted.

The output of the HOM interferometer is a secondorder correlation measurement, which can be mathematically described by the coincidence interferogram function [20]

$$C(\tau) = \frac{N_0}{4} \iint d\omega_1 d\omega_2 |f_{PM}(\omega_1, \omega_2) H(\omega_2)$$
$$- f_{PM}(\omega_2, \omega_1) H(\omega_1) e^{i(\omega_2 - \omega_1)\tau}|^2, \qquad (A8)$$

where N_0 represents the background coincidence count rate and $H(\omega)$ represents the sample transfer function. For a two-layer sample, this function is given by $H(\omega) = r_1 + r_2 e^{i\omega T}$, where r_1^2 and r_2^2 correspond to the reflectivities of the two layers and T represents the propagation time between them. By expanding each term, we obtain

$$C(\tau) = \frac{N_0}{4} [G_0 - G(\tau)],$$
 (A9)

where

$$G_0 = \iint d\omega_1 d\omega_2 [|f_{PM}(\omega_1, \omega_2) H(\omega_2)|^2 + |f_{PM}(\omega_2, \omega_1) H(\omega_1)|^2]$$
(A10)

are the self-interference terms that are independent of τ , and the cross-interference terms [11,20]

$$G(\tau) = \iint d\omega_1 d\omega_2 [f_{PM}(\omega_1, \omega_2) f_{PM}^*(\omega_2, \omega_1)$$

$$\times H^*(\omega_1) H(\omega_2) e^{-i(\omega_2 - \omega_1)\tau} + \text{c.c.}, \qquad (A11)$$

which contain information about the light reflected back from each of the internal layers of the sample and, therefore, about its axial morphology. By substituting Eq. (A6) in Eq. (A11) and after a few algebraic simplifications, we obtain

$$G(\tau) = 2\sum_{mn} \sum_{m'n'} \Lambda_{mn} \Lambda_{m'n'} e^{-\frac{(\Delta_{mn}^{+} - \Delta_{m'n'}^{+})^{2}}{2\sigma_{d}^{2}}} e^{-\frac{(\Delta_{mn}^{-} + \Delta_{m'n'}^{+})^{2}}{2\sigma_{d}^{2}}} \times \left[r_{1}^{2} \kappa(0) + r_{2}^{2} \kappa(T) + r_{1} r_{2} e^{-\frac{\sigma_{d}^{2}}{8} \left(\frac{T}{2}\right)^{2}} \right] \times \cos \left(\omega_{0} T + \frac{(\Delta_{m,n}^{+} + \Delta_{m',n'}^{+})}{2} \frac{T}{2} \kappa\left(\frac{T}{2}\right) \right],$$
(A12)

where we have defined $\Lambda_{mn} \equiv J_m(\beta_1)J_n(\beta_2), \ \Delta_{m,n}^{\pm} \equiv m\Omega_1 \pm n\Omega_2$, and

$$\begin{split} \kappa(\mathcal{T}) &= e^{-\frac{\sigma_n^2}{8}(\mathcal{T} - \tau)^2} \\ &\times \cos\left(\frac{(\Delta_{m,n}^- - \Delta_{m',n'}^-)}{2}(\mathcal{T} - \tau) - \Theta_{m',n'}^{m,n}\right), \end{split}$$

with $\Theta_{m',n'}^{m,n} \equiv (m-m')\theta_1 + (n-n')\theta_2$, as explained in the main text.

APPENDIX B: EXPERIMENTAL SETUP

Figure 2 shows the experimental setup for phase-dependent QOCT. In essence, the setup consists of the source of entangled pairs, the modified HOM interferometer, and the coincidence detection system. The system is pumped with a tunable CW laser, emitting light with a pump wavelength centered at $\lambda_0 = 404.5$ nm and set to an average power of

60 mW. The pump polarization and beam waist diameter are controlled with a half-wave plate and a planoconvex lens (L1, $f = 1000 \,\mathrm{mm}$), respectively, that have been set to maximize transmission and focus the beam to have a diameter of 300 µm. The pump feeds a 2-mm-long β -barium borate crystal, which generates pairs of entangled photons through type-I SPDC. The signal and idler photons are emitted noncollinearly at an exit angle of 3° with respect to the pump axis. The output is filtered with a long-pass filter with cutoff wavelength $\lambda =$ 500 nm, which blocks the pump and a spectral BPF centered at 800 nm, with a 40 nm width. The signal and idler photons are separated using a right-angle prism mirror that leads each of the twins into PMSMFs, which provide spatial mode filtering and ensure that the arms of the interferometer are fed with Gaussian modes. The output of the PMSMFs feeds the sample and reference arms of the interferometer.

The phase of each twin photon is independently modulated using EOMs placed at the output of the PMSMFs. These EOMs are low-loss lithium niobate phase modulators designed to operate around 795 nm. Each modulator is driven by a signal function generator, which provides a signal with adjustable amplitude, driving rf frequency, and phase difference relative to a common rubidium clock that serves as a reference. The SFGs have a maximum output frequency of 12.7 GHz and an output voltage of 7.24 Vpp (22 dBm), corresponding to a range of $\beta_1 \leq 5.42$ and $\beta_2 \leq 4.48$, since $V_{\pi_1} = 3.08$ V and $V_{\pi_2} = 3.73$ V. The values of β include a correction in input power due to cable losses.

The signal photon is directed to the reference arm, where a temporal delay is introduced using a system consisting of a PBS, a QWP that ensures the correct polarization for interference, and a translational mirror mounted on a motorized precision linear stage with a micrometer step size. The temporal delay τ is controlled by adjusting the path-length difference between the signal and idler photons.

In the sample arm, the idler photon probes a multilayered sample composed of two reflective interfaces. The sample used in our experiment is 2-mm-thick glass coated at the front and back with a thin gold layer via electron beam deposition. The reflectivities of the front and back layers (along the direction of light propagation) are 36% and 95%, respectively. The signal and idler photons are then recombined at a 50:50 beam splitter, which forms the core of the HOM interferometer. The output beams at the beam splitter's exit ports are coupled into avalanche photodiode (APDs). The normalized coincidence interferogram $\Gamma(\tau)$, resulting from HOM interference, is measured using a time controller unit with a fixed coincidence window of 2 ns.

The impact of phase modulation on artifacts in the QOCT trace is assessed by varying the phase of the entangled photons through adjustments to the EOMs' voltage or applied power, phase, and frequency. The resulting coincidence interferograms are recorded by independently varying EOMs parameters and performing a scan over the temporal delay τ (in ps), corresponding to the optical path length (in μm) traveled by light through the sample. An HOM dip appears in the event that the path-length difference between the reference and sample arms is zero ($\tau=0$), that is, when the idler photon is reflected back from a reflective interface within the sample. While the entire sample length is scannable, our focus is on

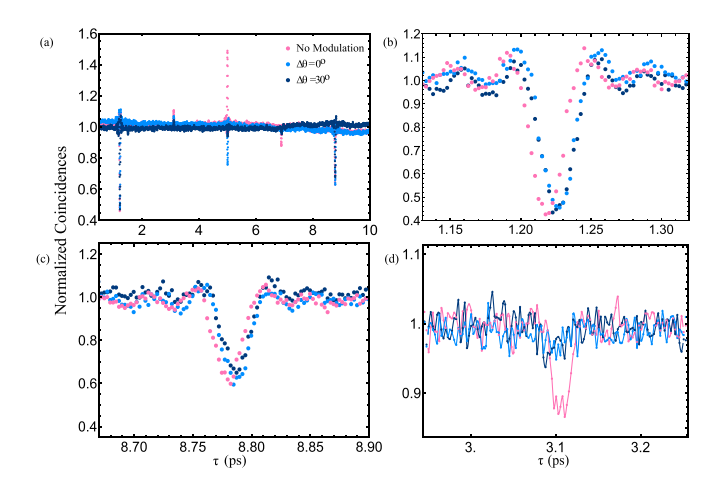


FIG. 5. (a) Full QOCT inteferograms of a 2-mm sample, with and without modulation. The interferogram shows two HOM dips corresponding to real interfaces and one artifact at the midpoint between them. Smaller artifacts appear due to an air gap in the sample acting as a layer. (b) A close-up of the first HOM dip, (c) a close-up of the second HOM dip, and (d) A close-up of the second small artifact in the experimental scan.

the region where the artifact appears. Additionally, the front and back surfaces are examined to confirm that the visibility of their respective HOM dips remains unchanged by phase modulation (see the Appendix). This is because the size of the sidebands, determined by the applied frequency and power, is much smaller than the bandwidth of the biphoton state.

APPENDIX C: FULL QOCT INTERFEROGRAM OF THE 2-MM SAMPLE

Figure 5 presents the complete interferogram of a sample of three interfaces, conducted to demonstrate the proof of principle for phase-modulated QOCT and to confirm that phase modulation does not affect the visibility of the HOM dips. Figures 5(b) and 5(c) present a close-up view of the first and the last HOM dips that show no change in their visibility, aligning with the theoretical model presented in the main text.

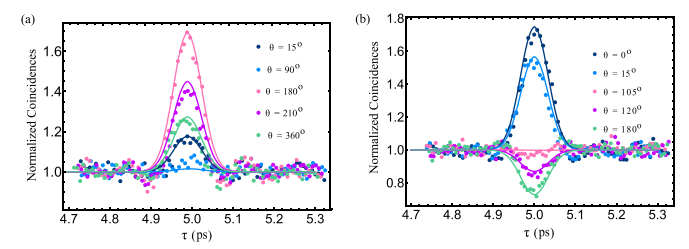


FIG. 6. The visibility of the artifact, measured in normalized coincidences, changing as a result of varying the phase of the EOM with (a) both EOMs fixed at $\Omega_1/2\pi = \Omega_1/2\pi = 6\,\text{GHz}$ and (b) both EOMs fixed at $\Omega_1/2\pi = \Omega_1/2\pi = 9\,\text{GHz}$.

The sample was fabricated by stacking two 1-mm-thick glass cover slips and depositing a thin gold film on their outer surfaces. The separation between the cover slips creates a thin air gap, introducing an additional layer with a reflective index of r=0.04. As a result, three artifacts appear in the interferogram: The main one at the midpoint between the front and back gold depositions and two smaller artifacts at $\tau=3.1$ ps and $\tau=7.1$ ps. While this behavior is consistent with our previous investigation of multilayered samples, the appearance of these smaller artifacts is not accounted for in the model presented in this work since it assumes a two-layer sample.

Nevertheless, these small artifacts, together with the main one, are removed by modulating the phase. Figure 5(d) shows a closer look at the first small artifact appearing at $\tau=3.1$ ps in the experimental scans. During the scans, the phase $\Delta\theta$ was varied, while the voltage and driving frequency were constant, $\Omega_1/2\pi=\Omega_2/2\pi=12.7$ GHz.

APPENDIX D: ARTIFACT REMOVAL WITH DIFFERENT DRIVE FREQUENCIES

Figure 6 shows scans of $\Delta\theta$ at different phases $\Delta\theta=15^{\circ}, 90^{\circ}, 180^{\circ}, 210^{\circ}, 360^{\circ}$. The driving signal was set to a constant voltage of 7.24 V and constant driving frequencies $\Omega_1/2\pi=\Omega_1/2\pi=6\,\mathrm{GHz}$ [Fig. 6(a)] and $\Omega_1/2\pi=\Omega_1/2\pi=9\,\mathrm{GHz}$ [Fig. 6(b)].

R. Horodecki, P. Horodecki, M. Horodecki, and K. Horodecki, Quantum entanglement, Rev. Mod. Phys. 81, 865 (2009).

^[2] N. Aslam, H. Zhou, E. K. Urbach, M. J. Turner, R. L. Walsworth, M. D. Lukin, and H. Park, Quantum sensors for biomedical applications, Nat. Rev. Phys. 5, 157 (2023).

^[3] S. Pirandola, B. R. Bardhan, T. Gehring, C. Weedbrook, and S. Lloyd, Advances in photonic quantum sensing, Nat. Photon. 12, 724 (2018).

^[4] S. Barzanjeh, S. Pirandola, D. Vitali, and J. M. Fink, Microwave quantum illumination using a digital receiver, Sci. Adv. 6, eabb0451 (2020).

^[5] S. Barzanjeh, S. Guha, C. Weedbrook, D. Vitali, J. H. Shapiro, and S. Pirandola, Microwave quantum illumination, Phys. Rev. Lett. 114, 080503 (2015).

^[6] R. Gallego Torromé and S. Barzanjeh, Advances in quantum radar and quantum LiDAR, Prog. Quantum Electron. 93, 100497 (2024).

^[7] T. D. Ladd, F. Jelezko, R. Laflamme, Y. Nakamura, C. Monroe, and J. L. O'Brien, Quantum computers, Nature (London) 464, 45 (2010).

^[8] A. W. Harrow and A. Montanaro, Quantum computational supremacy, Nature (London) **549**, 203 (2017).

^[9] C. Couteau, S. Barz, T. Durt, T. Gerrits, J. Huwer, R. Prevedel, J. Rarity, A. Shields, and G. Weihs, Applications of single photons to quantum communication and computing, Nat. Rev. Phys. 5, 326 (2023).

^[10] S. Wehner, D. Elkouss, and R. Hanson, Quantum internet: A vision for the road ahead, Science 362, eaam9288 (2018).

- [11] A. F. Abouraddy, M. B. Nasr, B. E. A. Saleh, A. V. Sergienko, and M. C. Teich, Quantum-optical coherence tomography with dispersion cancellation, Phys. Rev. A 65, 053817 (2002).
- [12] A. F. Fercher, W. Drexler, C. K. Hitzenberger, and T. Lasser, Optical coherence tomography—Principles and applications, Rep. Prog. Phys. 66, 239 (2003).
- [13] M. B. Nasr, B. E. A. Saleh, A. V. Sergienko, and M. C. Teich, Demonstration of dispersion-canceled quantumoptical coherence tomography, Phys. Rev. Lett. 91, 083601 (2003).
- [14] M. B. Nasr, B. E. A. Saleh, A. V. Sergienko, and M. C. Teich, Dispersion-cancelled and dispersion-sensitive quantum optical coherence tomography, Opt. Express 12, 1353 (2004).
- [15] B. I. Erkmen and J. H. Shapiro, Phase-conjugate optical coherence tomography, Phys. Rev. A 74, 041601 (2006).
- [16] S. Carrasco, J. P. Torres, L. Torner, A. Sergienko, B. E. A. Saleh, and M. C. Teich, Enhancing the axial resolution of quantum optical coherence tomography by chirped quasi-phase matching, Opt. Lett. 29, 2429 (2004).
- [17] M. B. Nasr, D. P. Goode, N. Nguyen, G. Rong, L. Yang, B. M. Reinhard, B. E. Saleh, and M. C. Teich, Quantum optical coherence tomography of a biological sample, Opt. Commun. 282, 1154 (2009).
- [18] P. Yepiz-Graciano, Z. Ibarra-Borja, R. Ramírez Alarcón, G. Gutiérrez-Torres, H. Cruz-Ramírez, D. Lopez-Mago, and A. B.

- U'Ren, Quantum optical coherence microscopy for bioimaging applications, Phys. Rev. Appl. **18**, 034060 (2022).
- [19] M. Y. Li-Gomez, P. Yepiz-Graciano, T. Hrushevskyi, O. Calderón-Losada, E. Saglamyurek, D. Lopez-Mago, V. Salari, T. Ngo, A. B. U'Ren, and S. Barzanjeh, Quantum enhanced probing of multilayered samples, Phys. Rev. Res. 5, 023170 (2023).
- [20] P. Y. Graciano, A. M. Martínez, D. Lopez-Mago, G. Castro-Olvera, M. Rosete-Aguilar, J. Garduño-Mejía, R. R. Alarcón, H. C. Ramírez, and A. B. U'Ren, Interference effects in quantum-optical coherence tomography using spectrally engineered photon pairs, Sci. Rep. 9, 8954 (2019).
- [21] P. Yepiz-Graciano, A. M. Martínez, D. Lopez-Mago, H. Cruz-Ramirez, and A. B. U'Ren, Spectrally resolved Hong—Ou–Mandel interferometry for quantum-optical coherence to-mography, Photon. Res. 8, 1023 (2020).
- [22] S. M. Kolenderska, F. Vanholsbeeck, and P. Kolenderski, Quantum-inspired detection for spectral domain optical coherence tomography, Opt. Lett. 45, 3443 (2020).
- [23] S. M. Kolenderska and M. Szkulmowski, Artefact-removal algorithms for Fourier domain quantum optical coherence tomography, Sci. Rep. 11, 18585 (2021).
- [24] S. M. Kolenderska, C. V. de Brito, and P. Kolenderski, Demonstration of Fourier-domain quantum optical coherence tomography for a fast tomographic quantum imaging, arXiv:2502.08372.